Chapter 2
Superconducting Transition Edge Sensors for Quantum Optics

Thomas Gerrits, Adriana Lita, Brice Calkins and Sae Woo Nam

Abstract High efficiency single-photon detectors allow novel measurements in quantum information processing and quantum photonic systems. The photon-number resolving transition edge sensor (TES) is known for its near-unity detection efficiency and has been used in a number of landmark quantum optics experiments. We review the operating principle of the optical superconducting TES, its use for quantum optics and quantum information processing and review its recent implementation in integrated photonic platforms.

2.1 Introduction

The superconducting transition edge sensor (TES) is an exquisitely sensitive device which exploits the abrupt change in resistance at the onset of the superconducting transition. Since its demonstration in 1998 [1] the optical TES has been improved and utilized by groups around the world and tailored for optical photon detection [2–6]. Owing to its intrinsic energy resolution capability, it is perfectly suited for the detection of optical pulses stemming from quantum optical processes in which the number of photons per pulse is needed to determine the state of the optical quantum system. Since interaction with the environment degrades every quantum system, detection of

T. Gerrits (✉) · A. Lita · B. Calkins · S.W. Nam
National Institute of Standards and Technology, 325 Broadway,
Boulder, CO 80305, USA
e-mail: thomas.gerrits@nist.gov

A. Lita
e-mail: adriana.lita@nist.gov

B. Calkins
e-mail: brice.calkins@nist.gov

S.W. Nam
e-mail: nams@boulder.nist.gov

R.H. Hadfield and G. Johansson (eds.), *Superconducting Devices in Quantum Optics*, Quantum Science and Technology,
DOI 10.1007/978-3-319-24091-6_2

optical quantum states must be done very efficiently, i.e. with as little loss as possible added by the detector. Thus the optical TES was continuously improved to achieve the highest detection efficiency possible, with efficiencies nowadays routinely in excess of ninety percent for fiber-coupled devices [7].

The detection of visible to near-infrared light is an important enabling technology for many emerging applications [8]. High optical intensities can easily be detected with room temperature devices, such as silicon photodiodes. These detectors can have high detection efficiencies close to 100 % and can detect light levels from tens of milliwatts down to picowatts (millions of photons per second). However, these devices are not capable of registering single photons. Photo-multiplier tubes (PMTs) had been and continue to be the workhorse for single-photon optical detection. However, their efficiencies are relatively low in the visible [8], and even lower in the telecom band at ∼1550 nm, where much of the current quantum information and communication technology is being developed. InGaAs avalanche photodiodes (InGaAs APDs) offer higher efficiencies (∼20 %) at telecom wavelengths. However, their dark count rates may be in the 100s of kilohertz. To mitigate this effect, their bias voltage is typically gated and synchronized with the expected optical input signal. This method of course precludes continuous quantum-state production techniques, and even then only offers incremental improvements in the effective detection efficiency and dark count rate. Currently the only available single-photon detectors offering high (near unity) detection efficiency paired with low dark count rates at telecom wavelengths are low-temperature superconducting devices. One of these is the superconducting nanowire single-photon detector (SNSPD). Najafi et al. give an introduction to SNSPD technology in Chap. 1 of this book; Chaps. 3, 4 and 5 expand on implementations and applications of SNSPD devices in quantum optics, information processing and communications.

This chapter gives an overview of the development and applications of superconducting transition edge sensors tailored for optical wavelengths. This work was principally carried out by the authors at the US National Institute of Standards and Technology (NIST) in Boulder, Colorado. We discuss the TES, its applications and future perspectives for single-photon and photon-number-resolved detection. We first review the operating principle of the TES, discuss techniques to improve the performance of these devices from the first demonstration, and describe techniques to characterize the performance of TES detector systems. Next we review important quantum optics experiments that benefited from the use of the TES. We also review our recent efforts on integration of TESs into optical waveguide circuits that will be used in future applications of TES detectors.

2.2 The Optical Transition Edge Sensor

2.2.1 TES Operation

2.2.1.1 Basic Operating Principle

Superconducting transition-edge sensors (TES) are highly-sensitive microcalorimeters that are used as microbolometers to detect radiation from sub-mm wavelengths to gamma-rays. They typically consist of an absorber, a sensitive thermometer, and a weak thermal link to a thermal bath [9]. The optical TES is a superconducting sensor measuring the amount of heat absorbed from an optical photon with energy on the order of 1 eV. When an optical photon is absorbed by the sensor, the associated photon energy is transformed into a measurable temperature change of the sensor. The most successful optical TESs operate at temperatures below 1 K [7, 10, 11]. However, higher operating temperatures are possible by reducing detector size (to maintain equal heat capacity of the electron system), even though light may miss the detector, reducing the system detection efficiency [12]. For devices operating below 1 K, the thermal isolation required is usually provided through the Coupling, electron-phonon within the superconductor itself, which can be weak at low temperatures, especially with certain superconducting metals. Tungsten is an example of a material which achieves the necessary weak coupling below its thin-film superconducting critical temperature T_c, typically $\sim$100 mK.

Due to the low photon energies involved, detection of single photons at optical and near-infrared wavelengths requires very low heat capacity and extremely sensitive thermometry. For optical TES detectors based on tungsten [7], the absorber is the electron system in the metal; the thermometer is the superconducting-resistive transition in the metal; the weak thermal link is the weak electron-phonon coupling in the metal itself; the thermal bath is the tungsten phonon system, strongly coupled to the lattice of the silicon substrate and, in turn, to the cryostat cold-plate onto which the detector chip is mounted [13].

2.2.1.2 Thermal Response

In our tungsten-TES detectors, after an optical photon is absorbed by an electron, the hot electron ($\sim$11, 000 K) scatters with neighboring electrons at a length scale equal to the mean free path. The thermal link between the electron and phonon system in tungsten is small compared to other metals, enabling strong non-equilibrium effects, in particular allowing for the electron system to remain hot for several hundreds of nanoseconds [14]. By contrast, a strong thermal link between the tungsten phonon system and the surrounding thermal bath allows immediate dissipation of the thermal energy into the thermal bath, a process much faster than the electron-phonon coupling, as shown in Fig. 2.1a. Thus the heat dissipation process can generally be

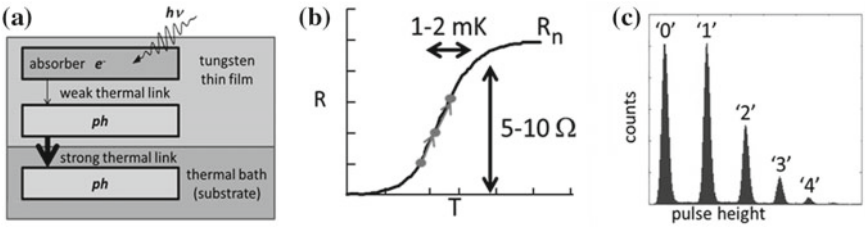

Fig. 2.1 The fundamentals of TES operation: **a** Principle of the TES as a microcalorimeter; **b** Resistance versus temperature "Transition edge" of a typical TES. Energy resolution is achieved by careful design of the system parameters; **c** Typical TES photon number histogram of amplitudes of the output response when illuminating the sensor with a weak coherent state

understood by a simple two-body model treating the phonon system of the tungsten and the thermal bath as one body:

$$C_e(T_e)\frac{dT_e}{dt} = \Sigma_{e-p}V\left(T_e^5 - T_{bath}^5\right) + P_J + \eta_\gamma \delta(t) P_\gamma, \tag{2.1}$$

where $C_\mathrm{e}(T_\mathrm{e})$ is the temperature-dependent heat capacity of the electron system ($C_\mathrm{e} = \gamma_\mathrm{e} \cdot V \cdot T_\mathrm{e}$); γ_e is the specific electron heat capacity coefficient, V is the absorber volume, T_e, and T_bath are the electron and thermal bath temperatures, $\Sigma_{\mathrm{e-p}}$ is the electron-phonon thermal coupling parameter, P_J is the Joule heating power due to the TES voltage bias, $\delta(t)P_\gamma$ is the absorbed optical power incident at the TES at initial time $t = 0$, and η_γ is the fraction of the optical energy transferred to the electron system after the optical pulse is absorbed with remainder being transferred to phonon system, i.e. η_γ is the energy collection efficiency. For tungsten, typical values are $\Sigma_{\mathrm{e-p}} \sim 0.4\,\mathrm{nW/(\mu m^3 K^5)}$, $\gamma_\mathrm{e} \sim 140\,\mathrm{aJ/(\mu m^3 K^2)}$ and $\eta_\gamma \sim 0.50$. During operation at the transition edge, the electron temperature is kept near the transition temperature via voltage biasing [15], i.e. $T_\mathrm{e} = T_\mathrm{c}$. The voltage bias causes Joule heating that raises the electron temperature of the detector to a temperature in the narrow superconducting-to-normal transition region, as shown in Fig. 2.1b. The transition edge is about 1–2 mK wide with a resistance change of several ohms. In steady state operation, the power dissipation of the device (Joule heating of the slightly resistive device) equals the power flow from the electrons in the tungsten to the phonons in the metal: $\Sigma_{e-p}V\left(T_e^5 - T_{bath}^5\right) = P_J = V^2/R(T)$. The positive temperature coefficient of resistance ($\mathrm{d}R/\mathrm{d}T > 0$), combined with the voltage bias, results in a negative electrothermal feedback that keeps the detector stably biased in the narrow superconducting transition. For example, if the temperature increases (decreases), the resistance increases (decreases), resulting in a smaller (larger) amount of Joule heating. With the detector thus equilibrated at a very steep point in its superconducting-to-normal transition, the absorption of a single photon results in a relatively large instantaneous change in the electrical resistance that can be measured with a Superconducting quantum interference device (SQUID) electronics described in the following section.

Figure 2.1b shows an example of a resistance versus temperature curve for a TES. Devices fabricated at NIST have a typical volume of 12.5 μm^3 (25 $\mu m \times 25\,\mu m \times 0.02\,\mu m$) and a transition temperature of $\approx$100 mK. A photon with an energy of 0.8 eV heats the electron system by $\approx$0.05 mK, resulting in a measurable resistance change. Due to the shape of the transition edge, an optical wave packet with some few numbers of photons will result in an increase in the resistance change of the device until the device approaches its normal resistance value. The response of the device to many such wave packets is shown in Fig. 2.3, where clear separation between different waveforms, corresponding to different numbers of absorbed photons, can be seen. A typical histogram of the different response pulse heights is shown in Fig. 2.1c. When operating the TES in the linear regime, the energy resolution determines the photon-number resolving capability of the detector (a monochromatic source is assumed). The energy resolution of the transition edge sensor is limited by the noise associated with the Johnson noise of the intrinsic resistance of the device, the noise associated with the statistical process of the electron-phonon thermal link [16] and the readout noise of the electronics. The TESs fabricated at NIST have a typical energy resolution of less than 0.25 eV in the linear operating regime [7].

2.2.1.3 SQUID Readout

The optical transition edge sensor readout is typically accomplished by use of superconducting quantum interference devices (SQUIDs) [17], which serve as low noise amplifiers of the current flowing through the TES. The SQUIDs are used to measure current flowing through coils that are inductively coupled to the SQUID loop (Fig. 2.2a shows the schematic of the TES readout). There are two coils. The one on the left couples signals from the TES (input coil), and the one on the right is used to optimize the output of the SQUID (feedback coil). Generally NIST optical

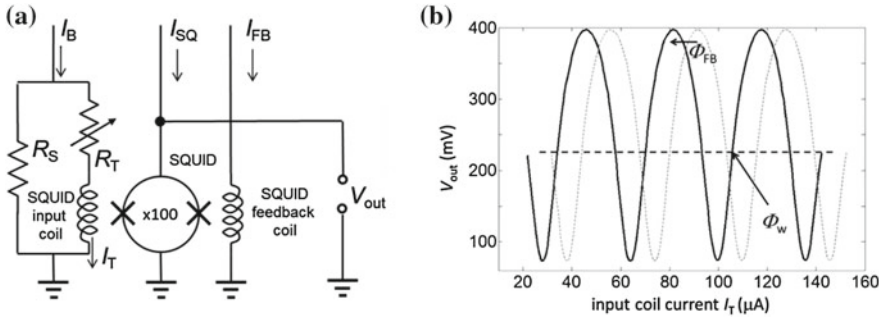

Fig. 2.2 TES readout via SQUID: **a** Schematic of the SQUID readout; **b** measured SQUID output voltage response (after x100 room temperature amplifier) as a function of input coil current (I_T) for $I_{FB} = 0$ (*dashed line*) and I_{FB} set to some value to maximize the TES response at it quiescent operating point (*solid line*)

TESs use a series array of SQUIDs, typically 100 (denoted by x100 in Fig. 2.2a), operating coherently [18] to produce signals large enough to be easily amplified at a later stage using simple room-temperature electronics. Because of the low operating temperature, and the need for a relatively stiff voltage bias, a small shunt resistor (R_s) is placed in parallel with the TES (the TES is drawn as a variable resistor (R_T) in the schematic). The value of R_s is chosen to be much smaller than the TES operating resistance when the TES is biased to detect photons ($R_s \sim 10\,\mathrm{m}\Omega$). The SQUID input coil inductively couples the TES current (I_T) via a magnetic flux (Φ_B) to the SQUID and therefore allows direct equivalent current readout.

Figure 2.2b shows a measured SQUID response as a function of feedback coil current. The period of oscillation is about $36\,\mu\mathrm{A}$, revealing a SQUID sensitivity of about $36\,\mu\mathrm{A}/\Phi_0$, where Φ_0 is the magnetic flux quantum. The amplitude of the oscillation is determined by the geometry and material of the SQUID's Josephson junctions. In this case, a x100 room temperature amplifier along with a x100 SQUID array was used. Consequently, the magnitude of the voltage swing of one SQUID itself is $\approx 32\,\mu\mathrm{V}$. The y-axis-offset originates from the resistance of the lead cable that supplies the bias current to the SQUID. For maximum signal-to-noise, the SQUID readout should operate around the maximum slope of the SQUID response, the working point. To accomplish this proper "flux bias," another coil is added to the SQUID, which inductively couples I_{FB} inducing flux Φ_{FB} to the SQUID. This added flux allows tuning of the overall flux through the SQUID, hence tuning the SQUID to the optimal working point: $\Phi_W = \Phi_B + \Phi_{FB}$.

2.2.1.4 TES Output

Figure 2.3 shows typical waveforms for a TES optimized for light at ≈ 800 nm wavelength. The TES was illuminated with weak coherent state pulses with a mean photon number per pulse of ≈ 2. The photon energy was 1.55 eV (800 nm). Detection efficiency of this particular device was found to be $\approx 94\,\%$ [13]. The figure shows 1024 individual waveforms of the TES response. Clearly, photon-number resolution is present, and up to 4 photons can easily be distinguished from the detector output. When no photon is present the signal consists entirely of the readout noise of the electronics, the Johnson noise of the detector itself and the fluctuations of the thermal bath [9]. The clear separation of the no-photon waveforms from those due to a photon means that the TES does not have any dark counts (false positives). There are however background counts. These background counts are real detections, which can be due to spurious visible wavelength photons coupled to the detector from the lab environment, spurious black-body photons or even high energy cosmic ray muons.

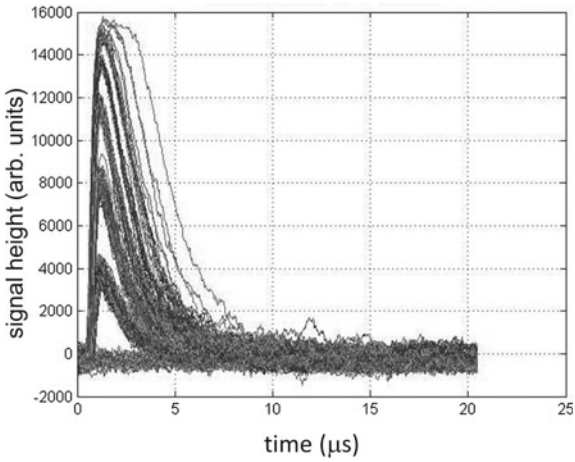

Fig. 2.3 Typical TES output $V_{\text{out}}(t)$ response waveforms under illumination with 1.55 eV (800 nm wavelength) photons

2.2.2 TES Optimization

2.2.2.1 Optical Stack Design

Absorption of optical photons in metals is generally dominated by the metal's interband transitions [19]. The interband transitions originate from the band structure of the metal. In principle, the optical absorption coefficient of a metal will be altered when the metal undergoes a superconducting transition due to a change of its band structure [20]. However, since this effect is small in tungsten, our studies show no significant change in the absorption coefficient when the tungsten undergoes the superconducting transition. A bare superconducting film is neither a perfect reflector nor highly absorptive at optical frequencies. For optical photons, the optical properties of the material can be well described using a complex index of refraction. At NIST, using the complex index of refraction for tungsten we have been able to embed a tungsten-TES in a dielectric stack with a quarter-wave back-short reflector, analogous to a microwave "backshort", to impedance-match the TES to free-space. The thickness of the dielectric layers can be varied to optimize the absorption at particular wavelengths. In general, it is possible to absorb >95 % of normal incident photons over a wide range of wavelengths from the UV to the mid-IR using variations of the dielectric stack layers optimized for a specific wavelength. The bandwidth of the absorption depends on the details of the stack design [7] (see Fig. 2.4a). A typical dielectric stack consists of a highly reflective mirror, a dielectric spacer, the active detector film and an anti-reflection (AR) coating.

A critical step in designing a multilayer structure that maximizes the absorption in a metal film is to determine the indices of refraction of all component layers. The optical properties of thin films differ from the bulk tabulated values, so it is necessary to measure the actual indices of refraction. The indices of refraction can be extracted from reflectance and transmittance measurements of thin-film samples deposited

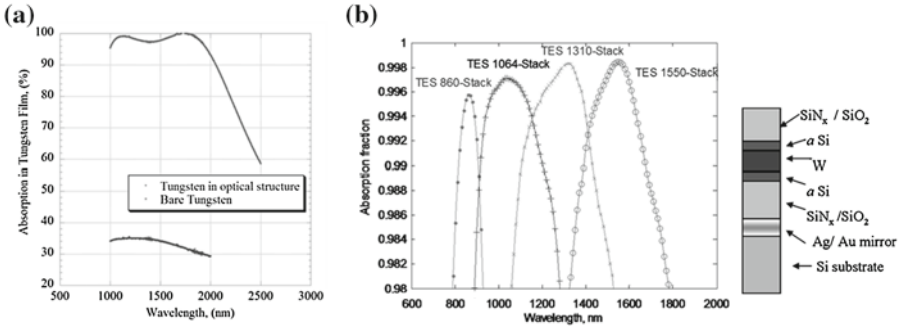

Fig. 2.4 Maximizing optical TES performance via optical cavity design: **a** Spectrophotometer data taken at room temperature indicating significant improvement in device absorption at 1550 nm when bare tungsten is embedded between appropriate dielectric layers; **b** Calculated absorption for tungsten (W) embedded in optical multilayer structure designed to optimize absorption at different wavelengths. (**a**) Reproduced with permission from Ref. [7]. Copyright 2008, Optics Express (OSA); (**b**) Reproduced with permission from Ref. [21]. Copyright 2010, Proceedings of SPIE

onto quartz or silicon wafers. Film thickness strongly influences the refractive index calculation and so must be measured with high accuracy. Using these measured indices of refraction for all layers in a thin-film modeling program, we designed structures that enhance absorption in the active device material. An optimization algorithm varies thicknesses for a fixed sequence of materials, and calculates the expected performance of the optical stack in terms of reflectance, transmittance, and absorption in the active device material. The component layer thicknesses giving maximum absorption in the active device material are used as target thicknesses when fabricating the optimized multilayer structure. The optical stacks for tungsten TESs designed at NIST are similar for all wavelength-specific designs (see Fig. 2.4b). The differences are in the layer thicknesses and the materials choice of non-absorbing dielectrics and/or top-layer AR coatings. Our simulations indicate greater than 99 % absorption in the tungsten layer at each target wavelength [21].

The bandwidth of the absorption depends on the details of the stack design. There are several important parameters to consider when designing optical stacks: thickness variation from design values to deposited layers in the structure, as well as interface intermixing or material reactivity can affect film optical constants and will shift the absorption of the multilayer stack from the design target value. Figure 2.5 shows how thickness variation from target values (output of the optimization algorithm) may affect the overall reflectance of the multilayer structure for a TES optical stack optimized for absorption at 810 nm. By employing a Monte-Carlo search algorithm randomly varying layer thicknesses within a standard deviation of 5 % from the target values, a better estimate of the actual measured absorption is obtained. The altered simulation curve represents the expected reflectance corresponding to slightly different layers thicknesses than designed, in this case 1 % to 7 % thickness variations for 4 out of 6 layers in the structure.

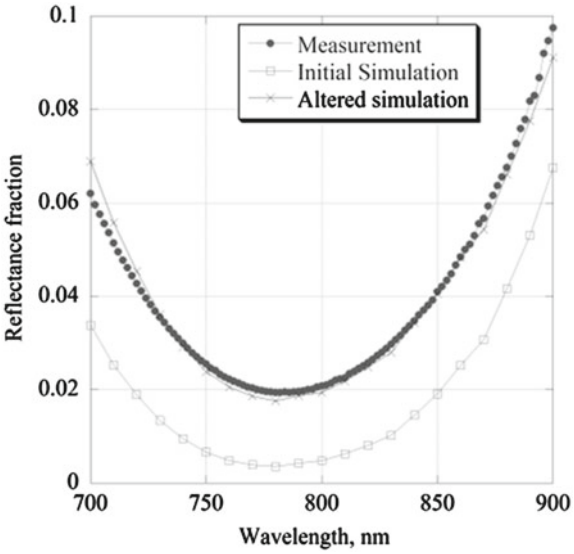

Fig. 2.5 The tungsten TES optical structure consisting of 6 layers is optimized for absorption at 810 nm wavelength. Reflectance curves for initial simulation (*open circles*), measurement (*solid circles*), and Monte Carlo altered simulation (*crosses*) are displayed. Reproduced with permission from Ref. [21]. Copyright 2010, Proceedings of SPIE

Compatibility of layers in the optical structure is also important, especially since stresses will arise from the differences in coefficients of thermal expansion when cooling down to the cryogenic operating temperatures, 100 mK to 200 mK. An example of incompatibility between layers is seen when hafnium (Hf) is used as a TES. When embedding Hf in a multilayer structure (mirror of gold, dielectric spacer Si_3N_4, Hf active device material, Si_3N_4 as antireflection coating), absorption in the active device material can be greater than 99 % at 860 nm [22]. However, stress induces a broadening in the superconducting transition of Hf in the multilayer structure. That broadening results in a significant increase in TES recovery time (20 μs for Hf in multilayer compared to ∼500 ns for the bare Hf) [22]. For tungsten TESs in multilayer structures, the tungsten is deposited as part of an *in situ* trilayer: amorphous-silicon / tungsten / amorphous-silicon, which was found to enhance and stabilize the tungsten T_c against thermal-stress-induced suppression [23]. Titanium (Ti), is another material used for optical TES. By embedding Ti in an optical structure consisting of successive layers of dielectric deposited by ion beam assisted sputtering (IBS), high detection efficiencies at 850 nm (98 %) and 1550 nm (84 %) with fast response and 25 ns timing jitter were reported [10]. However, oxidation of Ti and subsequent oxygen migration (even when Ti is embedded in the optical structure) results in degradation of superconductivity and changes in refractive index. By adding an *in-situ* Au layer (10 nm) on top of Ti (30 nm), simulations have shown that absorption larger than 99 % is possible when using an antireflection coating consisting of 11 dielectric layers [24].

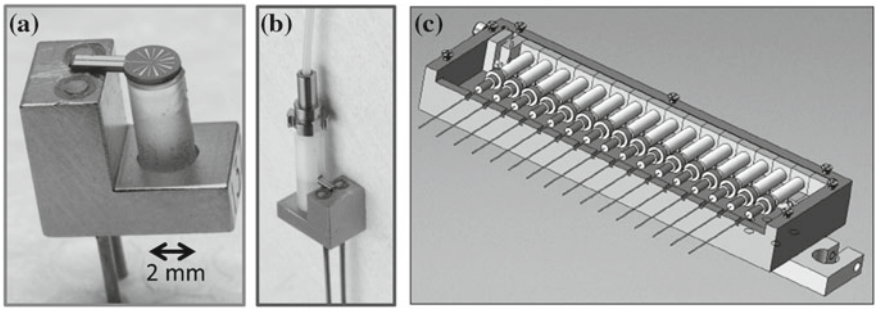

Fig. 2.6 TES packaging: **a** TES in self-aligned package; **b** TES package with optical fiber attached; **c** 16 channel detector mount box. Adapted from [13]

2.2.2.2 Detector Packaging

Reproducible and stable alignment of the optical fiber with the TES is crucial for reliably achieving high detection efficiencies. Since the optical-mode field diameter in the optical fiber is $\approx$10 μm, and the size of the TES is 25 μm $\times$ 25 μm, slight misalignment of the optical fiber with respect to the TES will result in decreased collection of optical photons onto the active area of the TES, and hence decreased overall detection efficiency. Also, a mechanically stable mount is required to allow for robust fiber-to-detector alignment that can survive multiple thermal cycling without drifting. Miller et al. [13] presented the self-alignment mount shown in Fig. 2.6. This shows the TES chip mounted on top of a sapphire rod held by a gold-plated oxygen-free, high heat-conductivity copper mount. The TES is located at the center of the 2.5 mm disk. Bond pads allow wire bonding the TES to gold pins integrated in the copper mount. A commercial zirconia fiber sleeve is put around the sapphire rod and TES chip (Fig. 2.6b). The TES chip and sapphire rod are precision machined to a diameter of 2.499 $\pm$ 0.0025 mm, such that the commercial fiber sleeve locates the TES precisely in the center of the sleeve. A fiber ferrule is inserted into the fiber sleeve. Both the fiber ferrule and sleeve have a combined specified tolerance of $\approx$1 μm. Along with the precision micro-machining of the TES chip this ensures fiber-to-detector alignment precision of about 3 μm [13]. Many of these self-aligned detectors can be compactly mounted together in a single unit (shown in Fig. 2.6c), which can easily be mounted in a cryogenic system.

2.2.2.3 Refrigeration of the TES

Since the TES are required to operate at temperatures below the temperature of liquid helium, elaborate cooling systems are required to operate these devices. The workhorse for operating the TES at around 100 mK temperatures is the adiabatic demagnetization refrigerator (ADR). The ADR relies on the magnetocaloric effect,

which manifests itself by cooling a paramagnetic material upon adiabatic demagnetization of that material, achieving temperatures of about 50 mK. In our case, the demagnetization process is initiated at temperatures around 4 K, given by the lowest temperature achievable by standard commercially available cryogenic cooling techniques. Since the total energy stored in the paramagnetic material is limited (about 1 Joule), the ADR only has a limited cooling capacity (or hold time). Due to the heat load via wires and optical fibers connected to the detectors, our ADRs generally have hold times of about 8–12 hours, depending on the number of TESs present. After the energy is depleted, the ADR temperature can be recycled, a process taking about 2 hours.

2.2.2.4 Speed Improvements and Timing Jitter

The recovery rate of the optical transition edge sensor is limited by the thermal link between the electron and phonon system. While a weak thermal link between the electron and phonon system is required for a photon to be converted to a detectable electrical signal, the weakness of this link can lead to long recovery times compared to other single-photon detectors such as superconducting nanowire single-photon detectors (SNSPDs) and single-photon avalanche photodiodes [8, 25]. The thermal recovery time of the TESs fabricated at NIST can be as short as 1–2 μs. During the thermal recovery time, the TES is still able to receive and detect a photon, and therefore has no dead time, which we note is unique among photon counting detectors. However, if an absorption event occurs during the recovery of the detector, signal pile-up will occur and will make the detector response characterization complicated. Thus, one seeks short recovery times to allow for high-repetition rate experiments. Calkins et al. have recently demonstrated such engineering of the thermal coupling between the electron and phonon system of the TES [26] achieving a thermal recovery time of less than half a microsecond.

Figure 2.7a shows a micrograph of a device fabricated with two $2\,\mu m \times 10\,\mu m \times 0.115\,\mu m$ gold bars deposited on the edge of the tungsten TES. Since the thermal

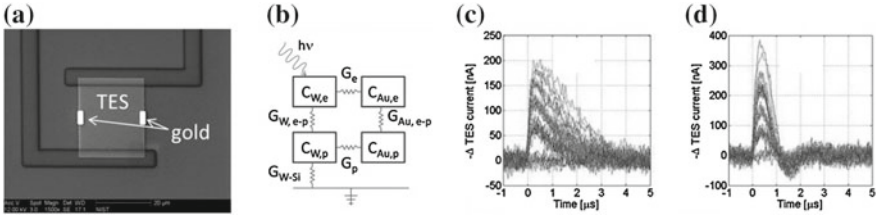

Fig. 2.7 **a** Micrograph of the fabricated TES with gold bars deposited on top of the tungsten; **b** Sensor electron-phonon coupling with the addition of gold bars; **c** TES response without gold bars; **d** TES response with added gold bars. Reproduced with permission from Ref. [26]. Copyright 2011, AIP Publishing LLC

electron-phonon coupling parameter of gold is ≈10x larger than for tungsten, one can engineer the thermal coupling by adding a controlled volume of gold to the TES. Figure 2.7b shows the thermal model of the TES with the gold bars added. The gold's electron system is strongly coupled to the tungsten's electron system. A strong thermal link $\Sigma_{\mathrm{Au,e-p}}$ between the gold's electron and phonon system allows for faster thermalization to the thermal bath, hence a modified thermal coupling constant of the whole system. In addition to the thermal coupling parameter, the strength of thermal coupling improvement depends on the gold's volume and its specific heat capacity coefficient γ_{Au} [26]. The difference in TES response with (Fig. 2.7d) and without (Fig. 2.7c) gold bars under illumination with an attenuated pulsed laser is easily seen. The TES with the gold bars reduced the thermal recovery time to ≈460 ns, an improvement of a factor of 4 without affecting the energy resolution [26].

In addition to faster recovery times, low timing jitter is another desirable parameter for most single-photon experiments [10, 27]. The timing jitter is the uncertainty in identifying the arrival time of the photon. It is important to realize that this is separate from the 'latency time' of the detector. Latency is the time delay from when the photon was absorbed by the detector to the time when the system indicates that a photon has been detected and is largely due to propagation delays in cables and amplifiers. The main contribution to timing jitter in TESs is noise in the identification of the time associated with the threshold crossing of electrical output pulse originating from a photon absorption event. The timing jitter (Δt_σ) of such an electrical signal can be approximated by:

$$\Delta t_\sigma = \frac{\sigma}{\frac{dA}{dt}|_t} \approx \frac{\sigma}{A_{\max}} \tau_{\mathrm{rise}}, \tag{2.2}$$

where σ is the root-mean-square (RMS) noise of the electrical signal, $\mathrm{d}A/\mathrm{d}t$ is the slope of the signal at a given time t, t_{rise} is the rise time and $A_{\max}$ is the maximum amplitude. The slope ($\sim \tau_{\mathrm{rise}}/A_{\max}$) of the electrical signal is directly proportional to the timing uncertainty of the electrical output. The rise time of the electrical signal for TESs used at NIST is generally limited by the overall inductance in the readout circuit and the resistance of the TES. In most of the experiments performed with NIST TESs, the combination of SQUID input inductance and wiring inductance leads to an inductance of a few hundred nH. This inductance along with the low TES resistance (≈1 Ω) will limit the signal rise time $\tau_{\mathrm{rise}} \sim L/R$ to several hundred nanoseconds. With a typical x100 SQUID amplifier, we measure a timing jitter full-width half maximum (FWHM) of ≈50–100 ns for the TES output, far greater than the timing jitter that would be required for a gated experiment using a Ti:Sapphire oscillator. Lamas-Linares et al. have recently demonstrated timing jitter FWHM values of 4.1 ns for 1550 nm single photons and 2.3 ns for 775 nm by directly wire-bonding the TES to a SQUID chip designed to have lower input inductance, and using high-bandwidth room-temperature amplification [27]. The lower timing jitter for higher energy photons stems from the larger amplitude of the TES output waveform.

2.2.3 Detector Characterization

2.2.3.1 Photon-Number Resolution

The optical TES is one of the few detectors with intrinsic photon-number-resolving capability. Other detection strategies exist where detectors with no number-resolving capability, 'click/no-click' detectors,[1] are multiplexed to achieve a quasi-photon number resolution. However, in those cases the fidelity of the measured state is always degraded compared to true/intrinsic photon-number-resolving detection. In many applications, however, multiplexed click detectors are sufficient to achieve high fidelity state characterization [28–30]. In contrast to simple 'click/no-click' detectors, the TES output contains information about the number of photons absorbed.

Figure 2.8a illustrates the photon-number-resolving capability of the TES. The TES was illuminated with weak coherent state pulses with a mean photon number per pulse of ≈2. The photon energy was 1.55 eV (800 nm). Figure 2.8a also shows a ≈2 μm wavelength black-body photon detection at ≈10 μs after the weak coherent pulses. When TESs are coupled to typical telecom optical fibers, background photons such as this result from the section of the high-energy tail of the room-temperature black-body emission spectrum that falls below the long cutoff wavelength of the fiber around 2000 nm [31]. However, when the energy of the signal photons is large enough, the black-body photons can easily be separated out by pulse height analysis. Generally, our TESs coupled to telecom optical fibers detect black-body photons at a rate of 500–1000 photons/sec^{-1}, which has a negligible effect on pulsed-light measurements and minimal effect on measurements of continuous sources in the near-IR down to the several femtowatt level. As can be seen in Fig. 2.8a, at higher photon numbers, the TES response enters the non-linear regime close to the normal conducting regime, and the photon-number resolution capability degrade.

To maximize the signal to noise ratio, post-processing of the output waveforms can be done. One fast, reliable method is optimum filtering using a Wiener filter [16]. Even though the optimum filtering method using Wiener filters only works in the case of white Gaussian noise (the TES response is not white due to the temperature dependent Johnson noise in the transition), the TES pulse heights can be reconstructed reliably with improved signal to noise ratio [7]. A measured coherent state with mean photon number of ≈5 is shown in Fig. 2.8b. In this case, the optimum filter analysis was used to determine the pulse-height histogram. Since the optimum filter makes use of a known linearly-scalable detector response, the method fails when the assumed detector response does not match the actual response, i.e. when entering the non-linear region. This effect is evidenced by the reduced visibility of the pulse height peaks for photon numbers larger than 4, shown in Fig. 2.8b. To improve the photon-number resolution at higher photon numbers in the non-linear region, one can find the most optimum representation of each photon-number response [32]. Also, linearization of the non-linear detector response can be accomplished to enable better

[1] We refer detectors with no photon-number-resolving capability as 'click/no-click' detectors, i.e. the detector cannot discriminate between the absorption of one or more photons.

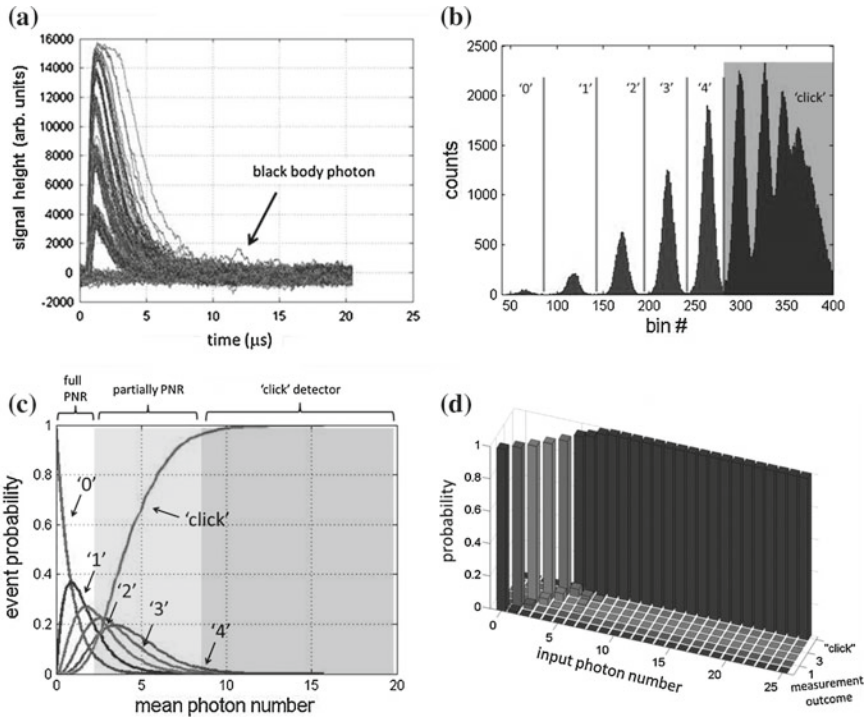

Fig. 2.8 Detector tomography results **a** Many TES output waveforms; **b** TES output pulse height histogram shown with boundaries dividing one detected number from the next; **c** Photon-number detection event probability as a function of input mean photon number; **d** Reconstructed POVMs for 0 through 4 photons and the "click" event

photon-number resolution close to or beyond the normal-conducting region [33]. Another method, allowing for analyzing detector responses far beyond the normal conducting regime was presented in Ref. [34] and will be presented below.

When characterizing the detector outcome for a photon-number-resolving detector one seeks to determine the probability of a detector response given a certain number of photons on the input. This probability is equivalent to the positive-operator-valued measure (POVM). The POVM characterizes the detector outcomes (in photon number k) for any given input photon number Fock state. Since pure photon number states at any value of k are still hard to realize in the laboratory, one employs a tomographic reconstruction of the POVMs based on measurement outcomes from excitation with weak coherent states, which are easily generated by attenuating a coherent laser beam [28, 35, 36]. Given a set of m coherent probe states C and a detector POVM Π, the measurement result R is given by: $R = C\Pi$. In general, POVMs are phase-dependent. However, in the case of TESs one can assume no phase dependence to the detector outcomes. Thus the POVM matrix is diagonal and can easily be represented by a vector. Also, in practice the Hilbert space needs to be truncated

at some photon number k_{max}. We chose detector outcomes 0 through 4 photons and define the 'click' outcome for photon numbers greater than 4. Figure 2.8c shows the detector outcome probability as a function of input coherent state mean photon number. For a given input mean photon number, we can identify three regimes: 1) Fully photon-number-resolving, where the probability of a click outcome is small; 2) Partially photon-number-resolving where a significant number of detector outcomes are 'click' outcomes; 3) 'click' detector where the majority of detector outcomes are above 4 photons. Figure 2.8d shows the POVMs reconstructed by the maximum likelihood reconstruction. These POVMs fully characterize the phase-insensitive detector response under the illumination with a k photon number state. In the case of the 1-photon outcome POVM, the POVM value at $k = 1$ yields the detection efficiency of the TES. A more complete tomographic reconstruction of the detector outcomes not relying on continuous POVMS instead of partitioning the outcomes for specific photon numbers, considers was recently presented in Ref. [37].

2.2.3.2 Extending the TES Response to the Normal-Conducting Regime

Transition edge sensors typically resolve photons over a range of 1 to 10 or 20, depending on the wavelength, heat capacity of the device, and steepness of the superconducting resistance transition. The severely reduced variation of resistance with temperature above the superconducting transition of the detector makes it more difficult to extract (or assign) photon numbers from detection events that cause saturation in the pulse height as illustrated in Fig. 2.8. Despite the saturation in the pulse height, one can still extract some information about the number of photons detected. The uncertainty in the number of photons detected may exceed one photon, but the number may be below the shot noise limit of the pulsed input coherent state. This sub-shot noise performance still could be useful in applications requiring weak light detection.

Figure 2.9a shows a TES response under illumination with a coherent state pulse with a mean photon number of 4.8×10^6 photons at a wavelength of 1550 nm [34]. The rise at $t = 0$ shows the initial heating of the electron system, and the TES immediately enters the normal-conductive regime, evidenced by the flat response out to

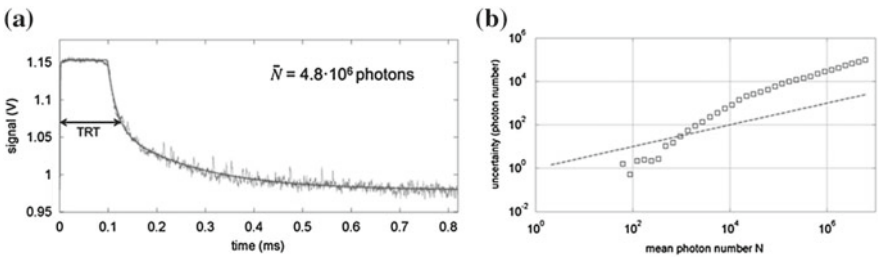

Fig. 2.9 **a** TES output waveform after excitation with about 4.8×10^6 photons in a single pulse; **b** uncertainty in photon number (*black squares*) after subtracting the photon source shot noise (*dotted line*) as a function of input mean photon number. Reproduced with permission from Ref. [34]. Copyright 2011, Optics Express (Optical Society of America)

0.1 ms. We can estimate the time it takes for the TES to return to its transition region (thermal relaxation time [TRT]) and use it to determine the initial heating of the electron system. A full fit to the detector response (dark solid line) yields the thermal relaxation time. Figure 2.9b shows the uncertainty in units of photon number as a function of input mean photon number derived from the TRTs. The black squares show the outcome uncertainty after subtracting the photon source shot noise. The uncertainties were obtained by determining the variance of the fitting parameters obtained from 20,480 waveforms for each input mean photon number. The dashed line shows the photon source shot noise. The results show that detection of ≈1,000 photons below the shot-noise is possible. Beyond 1,000 photons (≈1 keV) the uncertainty in the detector response rises above the input photon shot noise. The detector can reliably produce an outcome up to a mean photon number of ≈10,000 as outlined in ref. [34]. Beyond ≈10 keV the detector response deviates from the theoretical prediction due to cumulative heating of the detector substrate at the repetition rate of 1 kHz used in those measurements.

2.3 Applications of the Optical Transition Edge Sensor

2.3.1 Key Experiments in Quantum Optics

In this section we review experiments that have benefited from the high-detection efficiency and photon-number resolving capabilities of transition edge sensors (TESs). We review the first experiment using the TESs measuring the output photon-number statistics from a Hong-Ou-Mandel (HOM) interference experiment [38], describe how the TESs enabled us to generate high-fidelity coherent state superpositions (optical Schrödinger cat states) [3], and how subtraction of photons from a thermal state affects the photon-number distribution of the heralded state [39]. Lastly, we review fundamental tests of quantum non-locality that require high total detection efficiencies—detection-loophole-free Bell tests based on optical photons [40, 41].

2.3.1.1 Hong-Ou-Mandel Interference

HOM interference [42] lies at the heart of quantum interference and has been studied extensively over the last decades. The effect exploits the bosonic character of photons and forbids two indistinguishable single photons that enter two different input ports of a semitransparent beam splitter to exit different ports—the two photons will always exit either port together. To demonstrate or use this quantum interference, experiments usually rely on coincidence counting of single photons exiting the two output ports of the beam splitter. When full HOM interference exists (that is the two incident photons are completely indistinguishable), the coincidence rate should drop to zero. Using TESs, however, Di Giuseppe et al. were able to directly

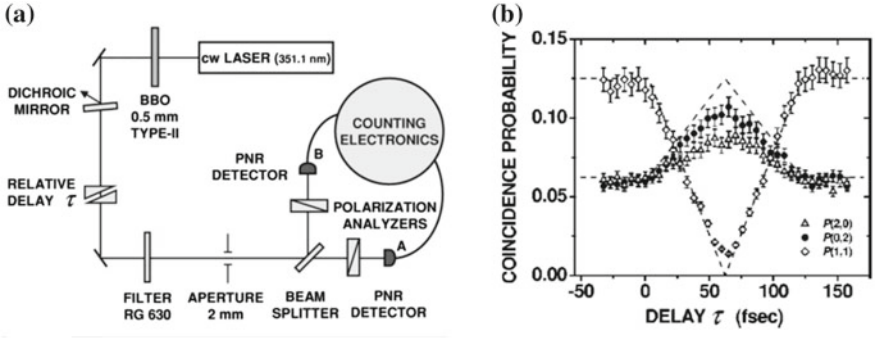

Fig. 2.10 **a** Setup for determining photon-number statistics from a Hong-Ou-Mandel experiment; **b** Measured Hong-Ou-Mandel interference dip and photon bunching. Reproduced with permission from Ref. [38]. Copyright 2003, Physical Review A (American Physical Society)

measure the photon-number statistics from a HOM beam splitter for the first time [38]. Figure 2.10a shows their experiment utilizing TESs for determining the output photon number statistics after HOM interference of two indistinguishable photons generated during a spontaneous parametric down-conversion event. The photons ($\lambda \approx 700$ nm) are delayed with respect to one another to observe the photon-number statistics as a function of the distinguishability of the photons' paths. Figure 2.10b shows the observed HOM interference dip (open diamonds), i.e. the probability of seeing one photon in one and one photon in the other output port, $P(1,1)$. As expected $P(1,1)$ approaches zero when both photons' paths become nearly indistinguishable. The open triangles and solid circles show the probability of two photons exiting one port, and no photon exiting the other port, $P(2,0)$, and vice versa, $P(0,2)$. In both cases the probabilities increase as the photon delay nears zero. This result showed the transition of a binomial (classical) distribution to a bosonic distribution of the two-photon state after interference on the beam splitter due to photon-number resolving capability of the TES.

2.3.1.2 Photon-Number Subtracted States

Photon-number subtraction is a useful technique for applications in quantum optics. One example of the use of photon subtraction is the generation of a coherent state superposition (CSS) state. Such states are often called Schrödinger cat states when each subsystem of the superposition contains a macroscopic number of photons. The use for high quality CSSs ranges from super-resolution metrology to quantum computing [43]. High fidelity CSSs are required to minimize the overlap between the two superimposed states and to achieve fault-tolerant quantum computing [44]. A number of experiments that aimed to generate such optical CSSs have been performed [45–48], two of which used TESs to herald the presence of the CSS [3, 48]. To create the CSSs a photon-subtraction scheme depicted in Fig. 2.11a is utilized, and

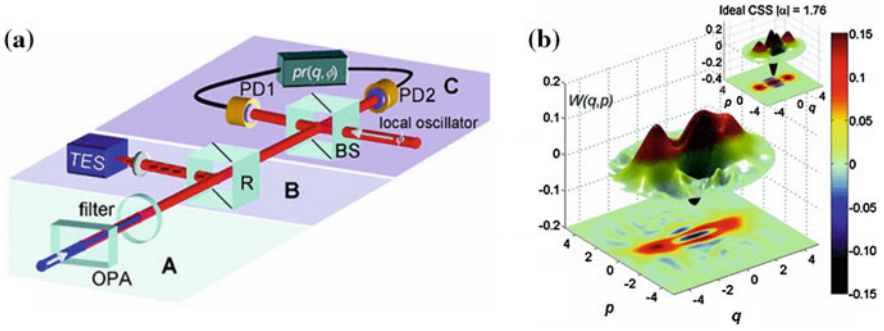

Fig. 2.11 **a** Scheme for optical Schrödinger cat state generation. An up-converted laser pulse enters an optical parametric amplifier (OPA) to create a squeezed vacuum state. After spectral filtering, photons are probabilistically subtracted via a weakly reflecting beam splitter and detected with a TES. Quadratures of the heralded state are measured by homodyne detection; **b** The reconstructed and theoretical cat state. Reproduced with permission from Ref. [3]. Copyright 2010, Physical Review A (American Physical Society)

we will concentrate in the following on the experiment performed in Ref. [3]. The scheme, in principle allows for large amplitude and high fidelity CSSs by heralding on the measurement of multiple photons subtracted from a squeezed vacuum [49, 50]. A squeezed vacuum state is prepared and sent through a weakly reflecting beam splitter. Reflected photons that are detected herald an approximate CSS in the transmitted beam. The TES used in this experiment had an efficiency of 85 % and was able to resolve up to 10 photons at a wavelength of 860 nm. The experiment aimed at generating the largest CSS with the highest fidelity. Figure 2.11b shows the theoretical and reconstructed Wigner functions of the CSS obtained after subtraction of three photons. The measured CSS had a mean photon number of 2.75 and a fidelity of 0.59, which remains the largest CSS generated from squeezed-vacuum photon-subtraction to date. Whilst the demonstration of large and high fidelity CSS was achieved, the rate at which these states were generated was low and made scaling impossible. However, recent work has demonstrated the potential for high-rate, high-fidelity approximations to CSS, through the use of photon replacement operations implemented with number-resolved detection [51].

Continuous variable (CV) quantum states, such as the CSS described above, are measured by use of optical-homodyne detection and reconstructed by maximum-likelihood estimation [52]. In this case, a strong local oscillator is used to determine the quadrature of the weak quantum field. Since the TES can resolve up to 20 photons, another method of measuring the quadrature of CV states is by performing optical homodyne measurements in the weak local oscillator regime, where the overall signal strength is on the order of the weak quantum state. A number of experiments have already been presented in the literature showing the capability of weak-field homodyne detection [53–55], one of which utilized the TES [56]. Combined with more efficient state generation schemes and because of the small amount of energy

absorbed by the detector, weak-field homodyne detection may become an important resource in the future when generating these states on-chip and mating them with high-efficiency superconducting integrated detectors [57–60], where low power dissipation platforms are a key challenge.

Another example of a photon-subtracted state was recently presented by Zhai et al. [39]. Up to eight photons were subtracted from a thermal state of light obeying Bose-Einstein statistics. A laser pulse illuminated a spinning disk of ground glass. Collection of the transmitted beam with a single-mode optical fiber selects a single-mode thermal state. By use of TESs, Zhai et al. reconstructed the photon-number statistics and showed that the photon number of the photon-subtracted state increases linearly with the number of subtracted photons. This seemingly counterintuitive result is explained by the noting that because thermal light is bunched, when sampling of a portion the light pulse made via the beam splitter finds a high number of photons, it means that the other portion of the light pulse (the other port of the beam splitter) is likely to also have a high number of photons. It is also important to note that these states, conditioned on the presence of a photon number larger than zero in the subtracted path, are necessarily rare because the photon-number probability always falls with increasing photon number. Given the measured photon number distributions, Zhai et al. also demonstrated that when using TESs, second- and higher-order correlation functions can easily be derived from the measured photon-number statistics [39, 61], and the thermal Bose-Einstein distribution approached a Poisson distribution representing the subtracted state when the number of subtracted photons is large.

2.3.1.3 Fundamental Tests of Quantum Non-locality

In classical physics, locality refers to the measurement outcome of an object that is influenced by its local interaction with the environment. To explain observed quantum mechanical correlations, an unknown theory that could describe the observed correlations at a local level may exist. Such a theory is referred to generically as a local hidden variable theory. Quantum Non-locality (QN) refers to the description of observed quantum mechanical correlations that cannot be mimicked by local hidden variable theories.

In 1964 Bell [62] developed an inequality showing that no local hidden variable theory can reproduce certain predictions made by using quantum mechanics. Bell's inequalities constrain correlations that systems governed by local hidden variable theories can exhibit, but some entangled quantum systems exhibit correlations that violate the inequalities. Thus, testing an inequality with a quantum system experimentally could falsify the hypothesis that the system is governed by a local hidden variable. However in all previous experiments, loopholes exist that a local hidden variable model can exploit to mimic the observed outcomes that violate the tested inequalities. These loopholes make an experimental test of local hidden variables a challenging endeavor. The three most prominent loopholes are the freedom of choice, locality, and detection (also called fair-sampling) loophole. While all loop-

holes have now been closed individually [40, 41, 63–66] with photons, an experiment addressing all of these loopholes simultaneously is still lacking. Here, we summarize experiments relying on the TES's high detection efficiency to close the fair-sampling loophole.

A variation of Bell's inequality based on a maximally polarization entangled state was introduced in 1970 by Clauser et al. [67], and an upper limit of ≈88 % for the overall detection efficiency of the entangled pairs necessary to close the fair-sampling loophole was introduced.[2] Even with the best detectors, such high overall system detection efficiency is difficult to achieve in photonic systems, since the entangled photons generally have to couple into single-mode optical fibers. This coupling can be lossy, although as it has recently been shown to be quite efficient (theoretically reaching almost 100 %) when considering the correct geometric coupling properties [68, 69]. Eberhard came to the conclusion that lowering the amount of entanglement of polarization entangled states, allows for lower overall system detection efficiencies, as low as 2/3 [70]. This absolute lower limit assumes no detector dark counts or degradation of the entanglement visibility. Thus, a system efficiency of >70 % is a more realistic efficiency to aim for.

Recently two groups succeeded in closing the fair-sampling loophole by use of photons and TESs [40, 41]. Both experiments made use of entangled photon pairs generated in a spontaneous parametric down-conversion (SPDC) process and a variation of the Bell inequality, the so-called CH Bell inequality [71]. In both cases a clear violation of the CH Bell inequality was shown with an efficiency allowing for detector background counts and entanglement visibility degradation. Christensen et al. employed a non-collinear entanglement scheme at a down-conversion center wavelength of ≈710 nm. The TES optimized for this study had a detection efficiency of ≈95 %. The symmetric single-mode fiber coupling efficiency of the entangled photons was > 90 %. Additional loss of ≈5 % was introduced at the single-mode fiber/telecom fiber interface splice (the telecom fiber is generally used for coupling photons to the optical TES). Further, spectral filtering added ≈7 % loss to the overall system performance, leading to an overall system efficiency of ≈75 %. Giustina et al. used an entangled SPDC source based on a Sagnac configuration and achieved an overall system efficiency of ≈73 % and 78 % in the two collection modes. The TESs in this study were optimized for a center wavelength of 810 nm and had a detection efficiency of ≈95 %. The latter experiment was performed using a continuous wave excitation of the SPDC process.

Progress continues toward implementing an experiment using photons that closes all loopholes simultaneously. In these experiments, both high-efficiency detection and good timing resolution is needed. Further analysis of data obtained in Ref. [41] showed that because of the continuous excitation of the SPDC process, the results are in principle subject to the coincidence-time loophole [72]. Even though a re-analysis of the data revealed that the experiment was not subject to the coincidence-time

[2] Note that overall detection efficiency is a product of all optical losses in transferring the photons from where they are generated to where they are detected and the detector's detection efficiency (see Sect. 1.1.1).

loophole [73], future loophole-free experiments will use pulsed sources to define every trial of the Bell test. Also, an improved TES timing jitter results in better rejection of background light. Better rejection of background light lowers the needed overall source-to-detector coupling efficiencies needed to perform a loophole-free experiment.

2.4 Integration of Optical TES on Waveguide Structures

We now present our recent efforts towards integrating optical TESs into optical on-chip architectures for scalable quantum information processing. We review the results presented in two publications [57, 58]. Integrated optics has become one of the leading technologies for generating and manipulating complex quantum states of light, since mode-matching, low-loss and small device footprints allow for more complex structures. A recent example of photon routing using integration to build complex networks is Boson sampling [74–77]. In these experiments the photon detection was done off-chip, which severely limited the number of modes that could feasibly be measured due to interface losses. Therefore, high-efficiency on-chip detection via evanescent coupling of the optical mode is key to realizing such large-scale optical quantum information and communication applications. Currently, a number of groups are pursuing integration of superconducting single-photon detectors on scalable platforms. Most efforts center around superconducting nanowire single-photon detectors [59, 60, 78–80]—two such approaches are reviewed in Chaps. 3 and 4 of this volume. Our method exploits integrated TESs which combine both high efficiency and intrinsic number resolution. Any integrated detector will avoid loss originating from coupling off-chip. In addition, such a detector can in principle be placed at arbitrary locations within an optical waveguide structure to allow optical mode probing, and allow in principle fast feed-forward operations, if all detection, decision, and photon routing is performed on chip. As we show, such a detector will also enable mode-matched photon-number subtraction without the need for complicated optical setups. However, one challenge remains when integrating source, circuit and detector on-chip. Since the number of pump photons required to generate single-photon states is large, a small fraction of the pump photons may leak into the single photon detector, resulting in unwanted detection events degrading the fidelity of the desired state. Therefore, pump filtering and pump rejection is currently one of the major challenges towards realization of a fully-integrated device.

2.4.1 On-Chip Transition Edge Sensor

For integration of our TES, we use a silica-on-silicon planar structure and UV laser writing to define the optical waveguide [81] fabricated at the University of Southampton (U.K.). Figure 2.12a shows the schematic of this structure. A thermal

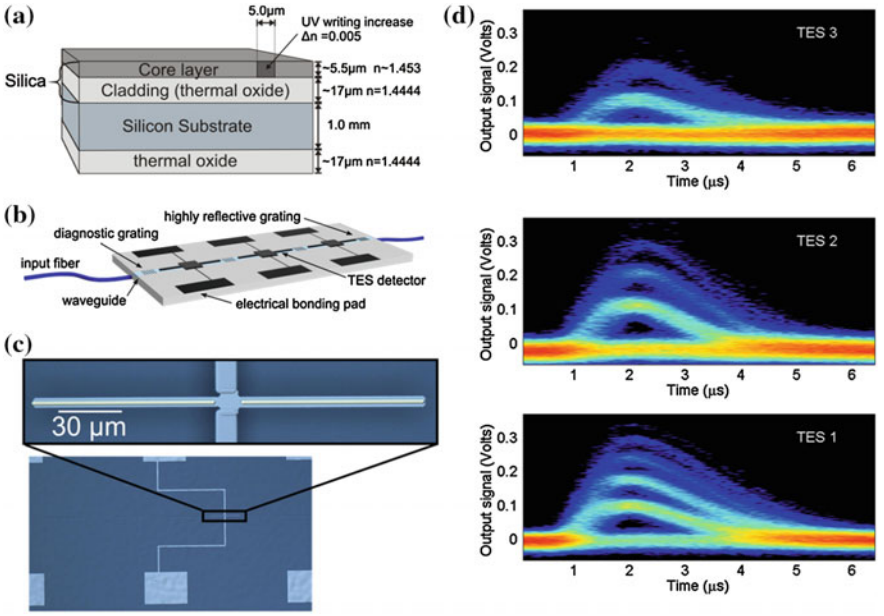

Fig. 2.12 **a** Schematic of the silica waveguide structure; **b** Schematic of the multiplexed long absorber evanescently coupled TES; **c** Micrograph of one fabricated long absorber TES; **d** Electrical output waveforms for all three multiplexed TESs. (**a**) Courtesy James Gates, University of Southampton, U.K. (**b**)–(**d**) Reproduced with permission from Ref. [58]. Copyright 2013, Optics Express (Optical Society of America)

oxide cladding layer is deposited on a silicon substrate. The waveguide core layer is a germanium-doped silica layer and deposited via Flame Hydrolysis Deposition (FHD). UV laser writing into the photosensitive core layer achieved an index contrast change of $\approx 0.3\,\%$ and results in a waveguide mode of Gaussian profile [82]. After UV writing, the optical waveguide is $\approx 5\,\mu$m wide. As a proof-of-principle we embedded a $25\,\mu\text{m} \times 25\,\mu\text{m} \times 0.04\,\mu$m TES on top of such a silica waveguide structure [57]. The detection efficiency of a photon inside the waveguide was found to be $\approx 7\,\%$. We found that when aiming for close-to-unity detection efficiency in such a silica waveguide structure, the evanescent coupling of the absorber has to be on the order of the length of 1 mm due to the small optical mode overlap with the absorber. In contrast, a silicon waveguide device with mode-field dimensions a factor of ten smaller than those of our silica device, only require $\approx 20 - 30\,\mu$m absorber length to achieve high absorption of the optical mode [60].

To improve the overall absorption and therefore the detection efficiency of our devices, we increased the absorber length and multiplexed three devices. Figure 2.12b shows the schematic of an integrated high-efficiency TES presented in Ref. [58]. The device consists of three detector regions with absorber lengths of $210\,\mu$m each, and yielded an overall device efficiency of $79\,\%$ for a photon inside the waveguide. This

approach used a separate absorber geometry increasing the interaction length with the optical waveguide mode. The total heat capacity of the absorber/sensor device was low enough to retain the photon-number resolution of the TES. A micrograph of the fabricated device is shown in Fig. 2.12c. The active TES is a 10 μm × 10 μm sensor made of tungsten, 40 nm thick operating at a transition temperature of ≈85 mK. Two 100 μm long tungsten absorbers are attached to the device and placed directly on top of the optical waveguide. To maintain an overall low heat capacity, the layer was 3.5 μm wide and 40 nm thick. A gold spine facilitates the heat conduction to the sensor area and allows the heat to reach the sensor region before being dissipated into the substrate. The gold layer was 2 μm wide and 80 nm thick. Simulations showed that for an absorber this length, the probability of absorbing a photon inside the waveguide should be ≈48 %. Simulations also revealed that the effective mode index mismatch at the absorber/no-absorber interface is on the order of 0.1 %. Therefore the optical mode is almost undisturbed, so reflections at the absorber/no-absorber interface are negligible. This allows multiplexing of several such detectors on a single waveguide to maximize the absorption of the optical mode. Calkins et al. also modeled the detector response due to the absorption of a photon along the long absorber [58]. When a photon is absorbed along the tails of these detectors, that energy must be transmitted to the sensor region before escaping via some other thermal path, e.g. through the phonon system into the substrate. This process is described by electron diffusion and depends on the thermal conductivity of the electron system and the amount of energy the electron system can carry. Calkins et al. found that a lower device temperature (lower T_c) and a large thermal conductivity are advantageous to facilitate such properties [58]. To maintain photon-number resolution, the maximum length of the absorber depends on the heat capacity, transition temperature, thermal conductivity, and electron-phonon coupling strength of the device. The latter will eventually leak heat out of the system into the substrate [58].

Figure 2.12d shows the waveforms from the device presented in Ref. [58]. A strongly attenuated pulsed 1550 nm laser was used to measure the device's response. The device consists of 3 individual detectors, TES 1 through TES 3. Clearly, photon-number resolution is well maintained for these long absorber detectors. Also, the measured detection efficiency was about 43 % per detector element, yielding an overall efficiency of ≈79 %. Figure 2.12d also shows the subsequent decay of photon-number amplitudes. Since all three detectors have the same length, each preceding detector absorbs part of the incoming photon state resulting in an exponential decrease in detected mean photon number with each additional detector. In this study all TESs were read out individually, each with a dedicated SQUID amplifier. This poses a scalability constraint when multiplexing many TESs on a single circuit.

2.4.2 A New Experimental Tool: On-Chip Mode-Matched Photon Subtraction

The experimental results, along with optical-mode modeling, allowed us to find the dependence of the detection efficiency as a function of the absorber length. We are now able to fabricate a detector with pre-determined absorption (detection efficiency). Since the silica platform requires relatively long absorbers per unit of detection efficiency, variation in the detection efficiency due to fabrication imperfections are considered to be small. This will allow us to implement the first quantum optics experiment utilizing the non-Gaussian operation of photon-subtraction on-chip, an experimental challenge when working with free-space optical components. Figure 2.13 shows a schematic of a heralded photon-subtraction experiment. This is similar to the scheme used for the generation of coherent state superpositions described above. A generated photon state is sent towards a beam splitter with known reflectivity. The beam splitter probabilistically reflects photons from the input state and sends it to a heralding photon detector. Measurement of a photon at this detector projects a subtracted photon-number state onto the input state. In this way, the transmitted (heralded) state can show non-classicality. The heralded state detection is accomplished by some other scheme such as homodyne detection or photon counting. The challenge in these kinds of experiments in free-space is to mode-match the photon subtraction (heralding) detector to the heralded state detection. The mode-matching must be done in the spatial, spectral and temporal regimes to achieve high-fidelity state generation. If the subtracted photon is not mode-matched to the heralded state detection, a vacuum state is detected, thus degrading the fidelity of the heralded state. The integrated approach, however, offers an almost perfect mode-matched heralding detector, since the optical mode transmitted matches the optical mode evanescently coupled to the heralding detector. Also, since the TES intrinsically has no dark counts, there should be no false heralding photon detection events. In addition, the TES has 100 % internal detection efficiency (probability of an absorbed photon yielding an output signal) for the subtracted photons. When combining the integrated photon subtraction scheme with weak-field homodyne detection, the integrated TES platform may become a powerful tool for the study and manipulation of optical quantum states.

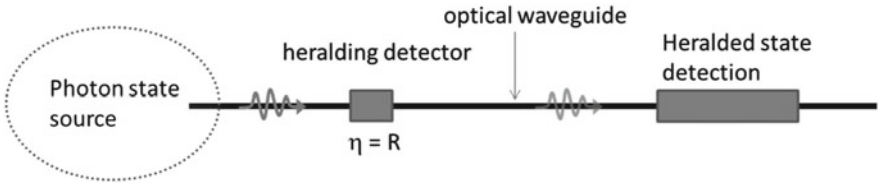

Fig. 2.13 Schematic of on-chip photon-number subtraction (heralding) for the experimental realization of non-Gaussian operations

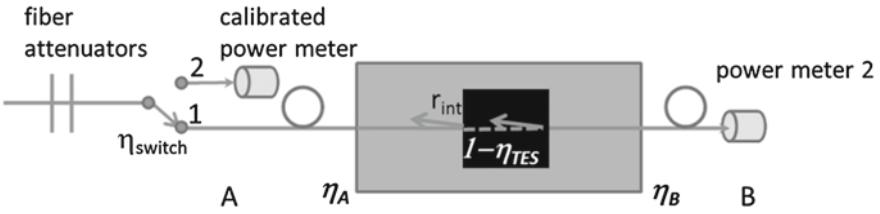

Fig. 2.14 Experimental scheme for measuring the coupling efficiency and detection efficiency of the TES detectors

2.4.3 On-Chip Detector Calibration

Determining the detection efficiency of a waveguide-integrated single-photon detector is a crucial aspect of studying the device performance. In contrast to fiber-coupled devices where the detection efficiency can be determined for photons inside the optical fiber, the overall detection efficiency of a waveguide-integrated detector also includes the fiber-to-waveguide loss, a non-negligible contribution to the overall device-loss. Here we show how we are able to discriminate between the fiber-to-waveguide coupling loss and the detection efficiency of a photon residing inside the waveguide, following the derivation found in the supplemental material of Ref. [57] and in [58]. Figure 2.14 shows the scheme for measuring the detection efficiency of the TES centered on top of the waveguide and simultaneously measuring the fiber-to-waveguide loss. We perform three independent measurements:

- We measure the overall transmission through the whole device. Under the assumption that fiber-to-waveguide coupling is single-mode, the coupling efficiencies at sides A and B are independent of the propagation direction of the photons. This assumption can easily be verified by measuring the transmission through the device in both directions: if $T = T_{\mathrm{AB}} = T_{\mathrm{BA}}$ then $T = \eta_{\mathrm{switch}}\eta_A(1 - r_{\mathrm{int}})(1 - \eta_{\mathrm{TES}})\eta_{\mathrm{B}}$, where η_{switch} is the switching ratio of the switch, η_{A} and η_{B} are the coupling efficiencies into the waveguide on side A and B, respectively. η_{TES} is the detection efficiency of the TES, and r_{int} is the reflection at the absorber/non-absorber interface. Since r_{int} is small ($\approx$0.1 %): $T \approx \eta_{\mathrm{switch}}\eta_A(1 - \eta_{\mathrm{TES}})\eta_{\mathrm{B}}$;
- We measure the overall system detection efficiencies including the fiber-to-waveguide coupling losses: $\eta_{sA/sB} \approx \eta_{\mathrm{A/B}}\eta_{\mathrm{TES}}$ (with $r_{\mathrm{int}} \ll 1$) for each propagation direction.

We can solve for η_{A}, η_{B} and η_{TES}. We can also estimate the uncertainty of the final outcome when including the calculated absorber/non-absorber boundary loss. It is important to note that this technique does not account for losses within the detection region, i.e. underneath the detector. These losses would be equivalent to a boundary reflection, and, if these are small they would only have small effects on the final detection efficiency outcome. We use two power meters to measure the overall transmission along both possible propagation directions (T_{AB} or T_{BA}). To achieve well-defined attenuated single-photon laser pulses, we calibrate optical fiber

attenuators using the calibrated power meter as outlined in Ref. [13]. The switch imbalance (ratio) is determined beforehand and is modeled according to a weak laser pulse propagating through a beam splitter with transmissivity η_{switch}. By this, we obtained: $\eta_{\text{A}} = 39.8\,\%$, $\eta_{\text{B}} = 47.9\,\%$ and $\eta_{\text{TES}} = 7.2\,\%$ for our first proof-of-principle device [57].

Similar to the method described above and in Ref. [57], the detection and fiber-to-waveguide efficiencies can be estimated for the high-efficiency multiplexed TESs. Calkins et al. determined the detection efficiency for all three multiplexed detectors also by measuring the overall system efficiencies for both propagation directions. In addition, they were also able to deduce the waveguide mode absorption in their estimation. In general the method yields $2N + 1$ measurements for N multiplexed detectors, allowing determination of more system parameters than necessary to extract the sensor and fiber-to-waveguide coupling efficiencies ($N + 2$). In principle, this method can be extended to many low-efficiency detectors allowing the probing of crucial circuit parameters, such as scattering losses, beam splitter ratios and detection efficiencies.

2.5 Outlook

We have given an overview of the superconducting optical transition edge sensor (TES) and its use in quantum optics experiments. The high detection efficiency of the TES combined with photon number resolving capability are key requirements for experiments in quantum optics and quantum information. However, it should be noted that the TES can in principle have a large dynamic range owing to its thermal response with low uncertainty. This large dynamic range at the single-photon level may be advantageous for calibration of photon pulses that are in the mesoscopic regime between single-photon detection and conventional sensitivities of semiconductor photodiodes. The relatively slow response and recovery time of the TES, particularly compared to superconducting nanowire single-photon detectors (Chap. 1), preclude their use in some high-speed photon-counting applications, but when true photon-number resolution is required, the TES is the most efficient tool to measure photon states across an extremely broad wavelength range. The almost unity detection efficiency of the TES is still unmatched and is crucial for fundamental tests of quantum nonlocality. We have presented our efforts on integration of optical TES on optical waveguide structures and showed a route towards high-detection efficiency implementation. A full source-circuit-detector implementation is still missing due to the challenges of optical pump reduction to minimize both the heat load on the cryogenic system and unwanted detection of spurious pump photons. However, circuit implementation, along with high-efficiency TESs, is on its way also investigating the potential for mode-matched high-efficiency photon subtraction for future quantum information applications.

In the future, the dynamic range of the TES may be interesting to studies that aim at macroscopic entanglement [83], a developing route of research that requires

single-photon resolution at levels of hundreds of photons. In principle, the energy resolution of the TES can be improved at the cost of speed, e.g. lower thermal heat escape mechanism. The combination of weak-field homodyne detection and integrated optics may lead to interesting, more complex experiments in the continuous variable regime of quantum optics.

Acknowledgments This work was supported by the Quantum Information Science Initiative (QISI) and the NIST *'Innovations in Measurement Science'* Program. The NIST authors thank all collaborators who enabled the joint experiments summarized in this chapter.

References

1. B. Cabrera et al., Detection of single infrared, optical, and ultraviolet photons using superconducting transition edge sensors. Appl. Phys. Lett. **73**, 735 (1998)
2. D. Rosenberg et al., Quantum key distribution at telecom wavelengths with noise-free detectors. Appl. Phys. Lett. **88**, 021108 (2006)
3. T. Gerrits et al., Generation of optical coherent-state superpositions by number-resolved photon subtraction from the squeezed vacuum. Phys. Rev. A **82**, 031802 (2010)
4. D. Rosenberg et al., Long-distance decoy-state quantum key distribution in optical fiber. Phys. Rev. Lett. **98**, 010503 (2007)
5. R.W. Romani et al., First astronomical application of a cryogenic transition edge sensor spectrophotometer. Astrophys. J. **521**, L153 (1999)
6. J. Burney et al., Transition-edge sensor arrays UV-optical-IR astrophysics. Nucl. Instrum. Methods Phys. Res. Sect. A: Accel., Spectrom., Detect. Assoc. Equip. **559**, 525–527 (2006)
7. A.E. Lita, A.J. Miller, S.W. Nam, Counting near-infrared single-photons with 95 % efficiency. Opt. Express **16**, 3032 (2008)
8. M.D. Eisaman et al., Invited review article: single-photon sources and detectors. Rev. Sci. Instrum. **82**, 071101 (2011)
9. K.D. Irwin, G.C. Hilton, *Transition-Edge Sensors, in Cryogenic Particle Detection* (Springer, Heidelberg, 2005)
10. D. Fukuda et al., Titanium superconducting photon-number-resolving detector. IEEE Trans. Appl. Supercond. **21**, 241 (2011)
11. L. Lolli, E. Taralli, M. Rajteri, Ti/Au TES to discriminate single photons. J. Low Temp. Phys. **167**, 803 (2012)
12. D.F. Santavicca, F.W. Carter, D.E. Prober, Proposal for a GHz count rate near-IR single-photon detector based on a nanoscale superconducting transition edge sensor. Proc. SPIE 8033, Adv. Photon Count. Tech. V **80330W**, (2011)
13. A.J. Miller et al., Compact cryogenic self-aligning fiber-to-detector coupling with losses below one percent. Opt. Express **19**, 9102 (2011)
14. B. Cabrera, Introduction to TES physics. J. Low Temp. Phys. **151**, 82 (2008)
15. K.D. Irwin, An application of electrothermal feedback for high resolution cryogenic particle detection. Appl. Phys. Lett. **66**, 1998 (1995)
16. D.J. Fixsen et al., Pulse estimation in nonlinear detectors with nonstationary noise. Nucl. Instrum. Methods Phys. Res. Sect. A: Accel., Spectrom., Detect. Assoc. Equip. **520**, 555 (2004)
17. R. Jaklevic et al., Quantum interference effects in Josephson tunneling. Phys. Rev. Lett. **12**, 159 (1964)
18. R.P. Welty, J.M. Martinis, A series array of DC SQUIDs. IEEE Trans. Magn. **27**, 2924 (1991)
19. C. Kittel, *Introduction to Solid State Physics* (Wiley, New York, 1956)
20. G. Dresselhaus, M. Dresselhaus, Interband transitions in superconductors. Phys. Rev. **125**, 1212 (1962)

21. A.E. Lita et al., Superconducting transition-edge sensors optimized for high-efficiency photon-number resolving detectors. Proc. SPIE 7681, Advanced Photon Count. Tech. IV **76810D** (2010)
22. A.E. Lita et al., High-efficiency photon-number-resolving detectors based on hafnium transition-edge sensors. AIP Conf. Proc. **1185**, 351 (2009)
23. A.E. Lita et al., Tuning of tungsten thin film superconducting transition temperature for fabrication of photon number resolving detectors. Appl. Supercond., IEEE Trans. **15**, 3528 (2005)
24. G. Fujii et al., Thin gold covered titanium transition edge sensor for optical measurement. J. Low Temp. Phys. **167**, 815 (2012)
25. R.H. Hadfield, Single-photon detectors for optical quantum information applications. Nat. Photon. **3**, 696 (2009)
26. B. Calkins et al., Faster recovery time of a hot-electron transition-edge sensor by use of normal metal heat-sinks. Appl. Phys. Lett. **99**, 241114 (2011)
27. A. Lamas-Linares et al., Nanosecond-scale timing jitter for single photon detection in transition edge sensors. Appl. Phys. Lett. **102**, 231117 (2013)
28. J.S. Lundeen et al., Tomography of quantum detectors. Nat. Phys. **5**, 27 (2009)
29. D. Achilles et al., Fiber-assisted detection with photon number resolution. Optics Lett. **28**, 2387 (2003)
30. T. Bartley et al., Direct observation of sub-binomial light. Phys. Rev. Lett. **110**, 173602 (2013)
31. D. Rosenberg et al., Noise-free high-efficiency photon-number-resolving detectors. Phys. Rev. A **71**, 061803 (2005)
32. Z.H. Levine et al., Algorithm for finding clusters with a known distribution and its application to photon-number resolution using a superconducting transition-edge sensor. J. Opt. Soc. Am. B **29**, 2066 (2012)
33. D.J. Fixsen et al., Optimal energy measurement in nonlinear systems: an application of differential geometry. J. Low Temp. Phys. **176**, 16 (2014)
34. T. Gerrits et al., Extending single-photon optimized superconducting transition edge sensors beyond the single-photon counting regime. Opt. Express **20**, 23798 (2012)
35. G. Brida et al., Ancilla-assisted calibration of a measuring apparatus. Phys. Rev. Lett. **108**, 253601 (2012)
36. B. Giorgio et al., Quantum characterization of superconducting photon counters. New J. Phys. **14**, 085001 (2012)
37. P.C. Humphreys et al., Tomography of photon-number resolving continuous output detectors. New J. Phys. **17**, 103044 (2015)
38. G. Di Giuseppe et al., Direct observation of photon pairs at a single output port of a beam-splitter interferometer. Phys. Rev. A **68**, 063817 (2003)
39. Y. Zhai et al., Photon-number-resolved detection of photon-subtracted thermal light. Opt. Lett. **38**, 2171 (2013)
40. B. Christensen et al., Detection-Loophole-free test of quantum nonlocality, and applications. Phys. Rev. Lett. **111**, 130406 (2013)
41. M. Giustina et al., Bell violation using entangled photons without the fair-sampling assumption. Nature **497**, 227 (2013)
42. C.K. Hong, Z.Y. Ou, L. Mandel, Measurement of subpicosecond time intervals between two photons by interference. Phys. Rev. Lett. **59**, 2044 (1987)
43. A. Gilchrist et al., Schrödinger cats and their power for quantum information processing. J. Opt. B: Quantum Semiclassical Opt. **6**, S828 (2004)
44. A.C. Lund, T.P. Ralph, H.L. Haselgrove, Fault-tolerant linear optical quantum computing with small-amplitude coherent states. Phys. Rev. Lett. **100**, 030503 (2008)
45. A. Ourjoumtsev et al., Generation of optical Schrödinger cats from photon number states. Nature **448**, 784 (2007)
46. A. Ourjoumtsev et al., Generating Optical Schrödinger Kittens for Quantum Information Processing. Science **312**, 83 (2006)
47. K. Wakui et al., Photon subtracted squeezed states generated with periodically poled $KTiOPO_4$. Opt. Express **15**, 3568 (2007)

48. N. Namekata et al., Non-Gaussian operation based on photon subtraction using a photon-number-resolving detector at a telecommunications wavelength. Nat. Photon. **4**, 655 (2010)
49. M. Dakna et al., Generating Schrödinger-cat-like states by means of conditional measurements on a beam splitter. Phys. Rev. A **55**, 3184 (1997)
50. S. Glancy, H.M. de Vasconcelos, Methods for producing optical coherent state superpositions. J. Opt. Soc. Am. B **25**, 712 (2008)
51. T.J. Bartley et al., Multiphoton state engineering by heralded interference between single photons and coherent states. Phys. Rev. A **86**, 043820 (2012)
52. A.I. Lvovsky, Iterative maximum-likelihood reconstruction in quantum homodyne tomography. J. Opt. B: Quantum Semiclassical Opt. **6**, S556 (2004)
53. K. Banaszek et al., Direct measurement of the Wigner function by photon counting. Phys. Rev. A **60**, 674 (1999)
54. K. Laiho et al., Probing the negative Wigner function of a pulsed single photon point by point. Phys. Rev. Lett. **105**, 253603 (2010)
55. G. Donati et al., Observing optical coherence across Fock layers with weak-field homodyne detectors. Nat. Commun. **5**, 5584 (2014)
56. N. Sridhar et al., Direct measurement of the Wigner function by photon-number-resolving detection. J. Opt. Soc. Am. B **31**, B34 (2014)
57. T. Gerrits et al., On-chip, photon-number-resolving, telecommunication-band detectors for scalable photonic information processing. Phys. Rev. A **84**, 060301 (2011)
58. B. Calkins et al., High quantum-efficiency photon-number-resolving detector for photonic on-chip information processing. Opt. Express **21**, 22657 (2013)
59. J.P. Sprengers et al., Waveguide superconducting single-photon detectors for integrated quantum photonic circuits. Appl. Phys. Lett. **99**, 181110 (2011)
60. W.H.P. Pernice et al., High-speed and high-efficiency travelling wave single-photon detectors embedded in nanophotonic circuits. Nat. Commun. **3**, 1325 (2012)
61. T. Gerrits et al., Generation of degenerate, factorizable, pulsed squeezed light at telecom wavelengths. Opt. Express **19**, 24434 (2011)
62. J.S. Bell, On the Einstein-Podolsky-Rosen paradox. Physics **1**, 195 (1964)
63. M.A. Rowe et al., Experimental violation of a Bell's inequality with efficient detection. Nature **409**, 791 (2001)
64. M. Ansmann et al., Violation of Bell's inequality in Josephson phase qubits. Nature **461**, 504 (2009)
65. J. Hofmann et al., Heralded entanglement between widely separated atoms. Science **337**, 72 (2012)
66. T. Scheidl et al., Violation of local realism with freedom of choice. Proc. Natl. Acad. Sci. **107**, 19708 (2010)
67. J. Clauser et al., Proposed experiment to test local hidden-variable theories. Phys. Rev. Lett. **23**, 880 (1969)
68. P.B. Dixon et al., Heralding efficiency and correlated mode coupling of near-IR fiber-coupled photon pairs. Phys. Rev. A **90**, 043804 (2014)
69. R.S. Bennink, Optimal collinear Gaussian beams for spontaneous parametric down-conversion. Phys. Rev. A **81**, 053805 (2010)
70. P. Eberhard, Background level and counter efficiencies required for a loophole-free Einstein-Podolsky-Rosen experiment. Phys. Rev. A **47**, R747 (1993)
71. J. Clauser, M. Horne, Experimental consequences of objective local theories. Phys. Rev. D **10**, 526 (1974)
72. J.Å. Larsson, R.D. Gill, Bell's inequality and the coincidence-time loophole. EPL (Europhysics Letters) **67**, 707 (2004)
73. J.-Å. Larsson et al., Bell-inequality violation with entangled photons, free of the coincidence-time loophole. Phys. Rev. A **90**, 032107 (2014)
74. M.A. Broome et al., Photonic Boson sampling in a tunable circuit. Science **339**, 794 (2013)
75. A. Crespi et al., Integrated multimode interferometers with arbitrary designs for photonic boson sampling. Nat. Photon. **7**, 545 (2013)

76. J.B. Spring et al., Boson sampling on a photonic chip. Science **339**, 798 (2013)
77. M. Tillmann et al., Experimental boson sampling. Nat. Photon. **7**, 540 (2013)
78. G. Reithmaier et al., On-chip time resolved detection of quantum dot emission using integrated superconducting single photon detectors. Sci. Rep. **3**, 1901 (2013)
79. F. Najafi et al., On-chip detection of non-classical light by scalable integration of single-photon detectors. Nat. Commun. **6**, 5873 (2015)
80. C. Schuck et al., Optical time domain reflectometry with low noise waveguide-coupled superconducting nanowire single-photon detectors. Appl. Phys. Lett. **102**, 191104 (2013)
81. A.S. Webb et al., MCVD planar substrates for UV-written waveguide devices. Electron. Lett. **43**, 517 (2007)
82. D. Zauner et al., Directly UV-written silica-on-silicon planar waveguides with low insertion loss. Electron. Lett. **34**, 1582 (1998)
83. V. Vedral, Quantifying entanglement in macroscopic systems. Nature **453**, 1004 (2008)

http://www.springer.com/978-3-319-24089-3

Superconducting Devices in Quantum Optics
Hadfield, R.H.; Johansson, G. (Eds.)
2016, XIII, 249 p. 110 illus., 84 illus. in color., Hardcover
ISBN: 978-3-319-24089-3